IEEE Open Journal of the
Industrial Electronics Society

Received 13 October 2023; revised 23 November 2023; accepted 28 November 2023. Date of publication 6 December 2023;
date of current version 12 January 2024. The review of this paper was arranged by Associate Editor Weiliang Xu.

Digital Object Identifier 10.1109/OJIES.2023.3339838

Spatially Highly Constrained Auxiliary Rotary Actuator for a Novel Total Artificial Heart

ROSARIO V. GIUFFRIDA [1] (Student Member, IEEE), RAFFAEL SENTI [1], DOMINIK BORTIS [1] (Senior Member, IEEE), TIM BIEREWIRTZ [2], KRISHNARAJ NARAYANASWAMY [3], MARCUS GRANEGGER [3], AND JOHANN W. KOLAR [1] (Fellow, IEEE)

[1]Power Electronic Systems Laboratory, ETH Zürich, 8092 Zürich, Switzerland
[2]Deutsches Herzzentrum der Charité, Institute of Computer-Assisted Cardiovascular Medicine, 13353 Berlin, Germany
[3]Department of Cardiac Surgery, Medical University of Vienna, 1090 Vienna, Austria

CORRESPONDING AUTHOR: ROSARIO V. GIUFFRIDA (e-mail: giuffrida@lem.ee.ethz.ch)

This work was supported by the SPARK program from the Berlin Institute of Health.

ABSTRACT In the context of a collaboration between the *Medical University of Vienna*, the *Power Electronic Systems Laboratory* of *ETH Zurich*, and *Charité Berlin*, the novel implantable total artificial heart *ShuttlePump* is currently being developed. Its novel low-complexity pumping concept requires a compact linear–rotary actuator (LiRA). The linear actuator (LA) part was designed, realized, and experimentally verified in previous work, and it can provide a peak axial force of about 45 N with about 8 W of continuous power dissipation. This article presents the details of the rotary actuator (RA) part. This has considerably lower output power requirements (about 100 mW) due to the low operating torque and angular speed (3.1 mN·m and up to 300 r/min, respectively). However, the RA is highly constrained spatially, as it needs to be integrated very close to the previously realized LA. This forces a permanent magnet synchronous machine (PMSM) design with a rotor only partially equipped with permanent magnets and stators covering only half of the total circumference, which introduces a considerable cogging component to the total torque. The proposed PMSM is, hence, optimized using finite-element method simulations to select a final design with low power losses and low cogging-induced angular speed ripple. The machine is realized as a hardware prototype, and the experimental measurements confirm that the proposed RA can meet the continuous torque requirement with 324 mW of power losses. The successful implementation of the RA (and LA) finally verifies the practical feasibility of the integrated LiRA and provides the basis for a comprehensive test of the complete *ShuttlePump* in a hydraulic test rig in the course of further research.

INDEX TERMS Artificial biological organs, permanent magnet machines, rotating machines.

I. INTRODUCTION

Concurrently with the progressive aging of the population in industrial nations, a steady increase in severe heart failure cases has been registered over the past few decades [1], [2]. Heart transplantation is the therapy of choice for heart failure patients, but the persistent shortage of heart donors remains the main limitation to address [3]. A promising alternative solution to completely replacing a failing heart is offered by total artificial hearts (TAHs). They are especially needed in all those cases where other mechanical circulatory support devices, such as left ventricular assist devices (LVADs), are not applicable, e.g., in the case of severe biventricular heart failure [4]. TAHs have been the subject of continued interest and research in the past few decades, with steady advancements and the development of numerous concepts [5], [6], [7], [8], [9], [10], [11], [12]. From the very first pneumatic and electromechanical concepts conceived to provide pulsatile blood flow [7], [8], [9], TAHs progressively incorporated rotary blood pumps in their design and turned into more compact and reliable devices [10], [11], [12]. Nevertheless, currently available TAH concepts still suffer from limited durability and/or relatively high complications rates, which can also be

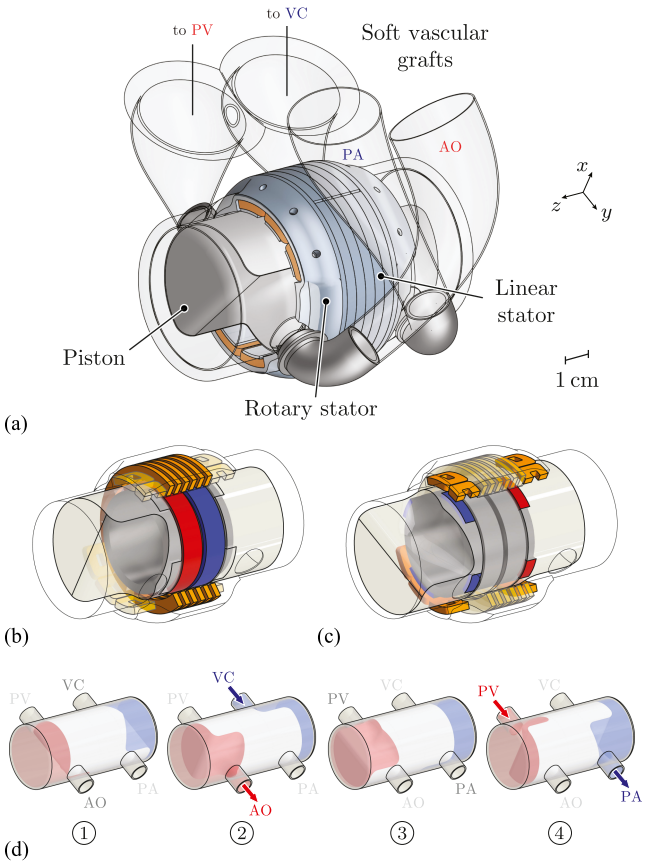

FIGURE 1. **(a) Implantable TAH *ShuttlePump*, connected via soft vascular grafts to the Aorta (AO), the Vena Cava (VC), the Pulmonary Artery (PA), and the Pulmonary Vein (PV). (b) LA part [17] of the LiRA system for the *ShuttlePump* highlighted. As the LA needs to deliver most of the mechanical power, it occupies most of the available volume. (c) RA part of the LiRA system highlighted. The RA is accommodated in the remaining volume after the LA is designed. (d) Operating principle of the *ShuttlePump*. The piston continuously rotates around the *z*-axis, controlling the opening/closing of the inlets/outlets and establishing a hydrodynamic journal bearing. During the left systole (stages 1 and 2), the piston translates along the positive *z*-axis, pushing the blood in the left chamber out while the right chamber fills up. During the right systole (stages 3 and 4), the translation direction is reversed, as well as the chambers being emptied/filled up.**

related to their complex design and limited hemocompatibility [13], [14]. As a matter of fact, in contrast to LVADs, their technology is not as mature, i.e., so far, no TAH has been approved for long-term treatment.

With the ambitious target of addressing the current limitations of TAHs, the *ShuttlePump* [cf. Fig. 1(a)] is proposed by Granegger et al. [15]. Its radically new low-complexity pumping concept offers a pulsatile physiological flow with only one moving part. The *ShuttlePump* is currently under development at the Power Electronic Systems Laboratory of ETH Zürich in partnership with *Charité Berlin* and the *Medical University of Vienna* [15], [16], [17]. The working principle of *ShuttlePump* relies on an specially designed piston following a combined linear–rotary motion [cf. Fig. 1(d)]. This is responsible for pumping blood in the systemic/pulmonary circulations while simultaneously opening/closing the pump's inlets and outlets, thus removing any need for prone-to-failure valves. The fluid-dynamic, clinical, and physiological aspects of the *ShuttlePump* have been studied at *Charité Berlin* and the *Medical University of Vienna* [16]. To enable the pumping operation, a *drive system* is needed, which consists of the electric machine serving as linear–rotary actuator (LiRA) [cf. Fig. 1(b) and (c)] together with the corresponding power electronics (inverter and control) unit.

The definition of an appropriate actuation concept and the subsequent design of the LiRA need to overcome several challenges due to the strict constraints and requirements that are defined for the *ShuttlePump*. These include, for instance, limitations in total volume, mass, and power losses to favor the system's implantability and prevent blood damage due to excessive heating. Such challenges have been tackled as a first step during the design and realization of the linear actuator (LA) part of the *ShuttlePump*, shown in Fig. 1(b) [17]. The LA occupies most of the available volume around the enclosure of the *ShuttlePump*, as it needs to deliver most of the mechanical power used to pump the blood into circulation. This article moves a step further in the development of the overall LiRA and the drive system by presenting the design, realization, and experimental verification of the rotary actuator (RA) part of the *ShuttlePump* [cf. Fig. 1(c)]. As the RA has the important yet auxiliary function of providing a constant rotation of the pump's piston, it needs to be accommodated in the remaining available volume close to the LA. The rest of this article is organized as follows. Section II summarizes the operating principle and characteristics of the *ShuttlePump* and defines the constraints and requirements for the RA. Based on these, Section III explains the proposed machine concept, and the appropriate machine topology is selected. The design is then optimized using finite-element method (FEM) simulations in Section IV, and the interactions with the LA are investigated. Section V provides details about the realized hardware prototype of the RA, which is verified experimentally with the results of Section VI. Finally, Section VII concludes this article.

II. SHUTTLEPUMP TAH AND DESIGN SPECIFICATIONS

This section summarizes the operating principle of the *ShuttlePump* and gives an overview of the spatial constraints and requirements that are defined for the RA.

A. OPERATING PRINCIPLE AND CHALLENGES

As the operating principle of the *ShuttlePump* is explained in detail in other related work [15], [16], only a compact summary is reported here for completeness. As visible in Fig. 1, the specially shaped piston divides the enclosure of *ShuttlePump* into two chambers, replacing the left and right ventricles. With a controlled linear–rotary motion conforming to the required hydraulic force and torque, the pumping operation is achieved. This can be visualized with the help of Fig. 1(d). During the linear motion, the blood is pushed out of one chamber (systole), while new blood is collected in the

TABLE 1 Specifications of the *ShuttlePump*, Extended From [17]

Name	Symbol	Value	Unit
Maximum axial dimensions	l_{ax}	105	mm
Maximum radial dimensions	d_{out}	70	mm
Piston axial length	l_p	78	mm
Piston outer diameter	d_p	48.72	mm
Inter- in-/outlets distance	l_{mid}	40	mm
Enclosure thickness (lateral)	d_{encl}	0.5	mm
Blood gap	d_{bg}	140	um
Magnetic gap	$d_{ag,min}$	1	mm
Maximum axial force	$F_{req,peak}$	≈ 43	N
Axial torque	M_{req}	3.1	mN m
Maximum radial force	$F_{rad,max}$	25	N
Piston weight	m_{mov}	< 300	g
Piston frequency	f_{op}	1.5 - 5	Hz
Piston rotational speed	Ω_{op}	90 - 300	rpm
Maximum speed ripple	$\Delta\Omega_{op}$	< 20	%
Operating conditions		2.5 - 9	L/min
Maximum Average Continuous Losses	$P_{Cu,avg,max}$	10	W
Blood temperature increase	ΔT_{max}	2	K

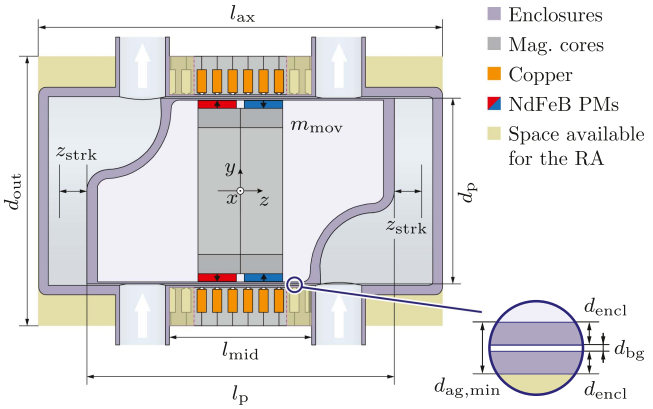

FIGURE 2. Sectional view (*yz*-) of the *ShuttlePump*, showing its enclosure and specially shaped piston with annotated dimensions, reported in Table 1. The designed LA is also visible, consisting of the stator (with the machine winding, around the enclosure) and the "translator" (with PMs, embedded in the piston) [17]. The yellow area indicates the available space that can be used to fit the RA. Importantly, the stator extensions of the LA can also be used for this purpose.

other. The rotary motion instead serves two important functions. On the one hand, according to the shape of the piston, it controls the opening and closing of the inlets and outlets. On the other hand, continuous rotation at a frequency of at least 1.5 Hz establishes a hydrodynamic journal bearing, which supports the piston radially during operation. The design of the drive system enabling such operation is challenging, not just because of the combined motion to control accurately. It is also due to the many limitations and requirements imposed by the application, some of which are reported in Table 1. Among these, the most critical is the axial force requirement on the linear motion, peaking at $F_{req,max} = 43$ N, which has to be generated with the least ohmic losses and in the least volume. In fact, the maximum allowed continuous ohmic losses are limited to $P_{Cu,avg,max} = 10$ W to comply with the regulations for active implantable devices, which indicate a limit of $\Delta T_{max} = 2$ K for local blood temperature increase [16], [18]. The volume, instead, is limited by the outer allowed dimensions of the *ShuttlePump*, determined with virtual fitting studies to ensure that implantation in a human subject is possible [16].

B. SPATIAL CONSTRAINTS AND REQUIREMENTS FOR THE RA

An inherent characteristic of the system is the high imbalance in the mechanical output power required from the LA and the RA. In particular, owing to the high axial force required to push the blood into circulation, the LA requires $P_{mech,avg,LA} = 3.6$ W on average during operation. In contrast, for the RA, the continuously required axial torque, obtained from computational fluid dynamics simulations, is $M_{req} = 3.1$ mN·m [16], and it is relatively low. Together with a rotational speed $\omega_{op,max} = 2\pi f_{op,max} = 31.42$ rad·s^{-1}, it results in an average mechanical output power of only $P_{mech,avg,RA} = 98$ mW. Consequently, it was decided to design the two actuators independently, prioritizing the LA instead of selecting a combined LiRA topology [19], [20], [21]. Therefore, as can be seen by comparing together Fig. 1(b) and (c), most of the available volume is utilized by the LA. The characteristics of the designed LA [17] are reported in Appendix A. The RA has to be accommodated in the remaining space, highlighted in Fig. 2. Both the actuators consist of a fixed stator hosting the machine winding and a moving part equipped with permanent magnets (PMs). For the sake of clarity, in this article, the moving part of the LA is denominated as the "*translator*," whereas the moving part of the RA is the "*rotor*." Together, they build up the "*mover*" of the LiRA, which is embedded in the moving "*piston*" of the *ShuttlePump*. The term mover refers to the magnetic element that interacts with the stators of the LiRA, whereas the term piston refers to the complete mechanical/hydraulic element (i.e., including the blades). The maximum outer diameter of the RA is limited as for the LA to $d_{out} = 70$ mm. Nevertheless, if possible, a design with a smaller diameter should be preferred, as it makes the overall system easier to implant. The stator of the RA will have to be placed on either side of the *ShuttlePump* or on both, within the maximum axial length of $l_{ax} = 105$ mm. Importantly, the stator extensions of the LA can also be modified for this purpose. The rotor of the RA will have to use the available surface of the piston, i.e., not already occupied by the PMs of the LA.

Compared to the LA, the requirements on the RA are less stringent altogether. Concerning the power losses, it is surely convenient to minimize them in order not to generate additional heat in the pump. However, it can be expected that the losses from the RA will only be a small share of the total. Moreover, the candidate locations for the RA are more favorable in terms of heat dissipation. In fact, unlike the thin blood layer right in the magnetic air gap of the LA, the two chambers host a large blood volume that continuously circulates through the pump, which is much more favorable for cooling. As a design guideline, a loss budget of $P_{Cu,RA,max} = 0.5$ W is

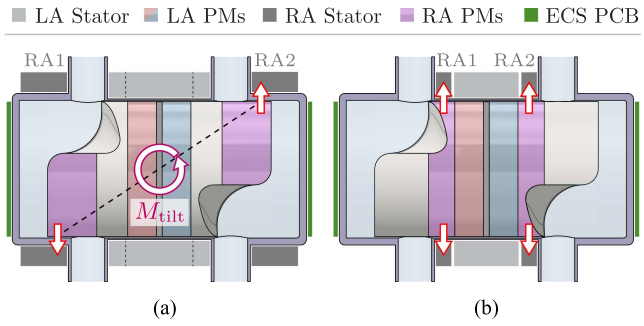

FIGURE 3. Two possible placement options for the two RA modules. (a) Option 1: toward the outer sides of the *ShuttlePump*. This option introduces an undesired tilting torque M_{tilt} due to unbalanced reluctance attraction forces at the two sides of the piston. Furthermore, the RA stators could disturb the eddy-current sensors (ECSs) mounted on the sides. (b) Option 2: toward the middle part of the *ShuttlePump*. With this option, a symmetrical design is possible, thus preventing any undesired tilting torque.

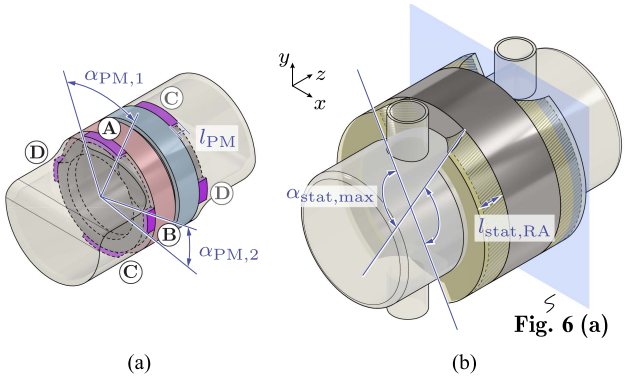

FIGURE 4. Proposed RA concept for the *ShuttlePump*. (a) 3-D view of the piston with designated locations (A to D) for the rotary PMs (purple), constrained to the limits $\alpha_{PM,1} = 45°$, $\alpha_{PM,2} = 25°$, and $l_{PM} = 5$ mm. (b) 3-D view of the enclosure with selected locations for the rotary stator highlighted in yellow. The stators are mostly integrated in the extensions of the LA and their length along the z-direction is $l_{stat,RA} = 12$ mm. Along the circumferential direction, they are constrained to $\alpha_{stat,max} = 110°$ on each side.

defined, which corresponds to 5% of the maximum allowed losses $P_{Cu,avg,max}$. Analogously, eventual magnetic pull forces that act radially on the rotor and disturb the hydrodynamic bearing are not considered, as they are negligible compared to the ones already introduced by the LA. Finally, certain RA designs can introduce cogging torque components due to, e.g., a slotted stator or edge effects. This leads to a certain speed ripple $\Delta\Omega$, which, however, is uncritical as long as $M_{req} = 3.1$ mN·m is provided on average. Considering further that the RA will be operated with an angular speed controller, an open-loop speed ripple up to 20% of the operational speed Ω_{op} can be allowed. This aspect is discussed more in detail in Section III-C, once the RA concept and topology are defined.

III. PROPOSED MACHINE CONCEPT

This section presents the proposed machine concept for the RA, according to the considered spatial constraints. Similarly to the LA, this is also based on a permanent magnet synchronous machine (PMSM) with surface-mounted PMs. To keep the system's complexity as low as possible, the number of phase currents of the RA will be limited to three. Together with the three phase currents of the LA, the complete LiRA features a total of six phase currents.

A. PLACEMENT OF THE ROTARY PMS AND STATORS

Given the tight space constraints and the geometry of the *ShuttlePump*, it is decided to realize the RA out of two modules, located on the two sides of the pump. This way, the total functional volume of the RA can be more evenly distributed around the pump compared to when a single RA module is used. Considering the presence of the pump's inlets and outlets, there are two main placement options for the two RA modules, illustrated in Fig. 3.

The first option is to place them toward the outer sides of the pump, as shown in Fig. 3(a). Although this way, most of the lateral surface of the two piston blades can be used to place the rotary PMs, there is one important drawback to consider. With this asymmetric design, there are two unbalanced net reluctance forces (acting between the PMs on the piston and the facing rotary stators, as indicated) along two offset planes, which cause an undesired tilting torque M_{tilt}. For small air gaps of the RA (typically beneficial for efficient machine designs), the magnetic attraction forces are strong, to the point that M_{tilt} could compromise the pump's operation. One possible work-around would be to choose a machine design with a large magnetic air gap (e.g., slotless), which, however, would require higher ohmic losses and/or a larger stator volume for the same torque output. Finally, another aspect to consider is that the chosen location for the linear–rotary position sensors will be on the two sides of the pump [22]. Owing to their eddy-current-based operating principle, no conductive material besides the piston-embedded measurement target is allowed in close proximity.

The second option overcomes the aforementioned drawbacks and is, therefore, the selected RA concept. As shown in Fig. 3(b), both the modules are placed toward the middle part of the pump, i.e., right adjacent to both the sides of the designed LA. The first and foremost advantage is that the stators of the RA can, thus, be integrated into the stator extensions of the LA. This allows us to beneficially reuse the excess core material that has to be placed anyway to guarantee the functionality of the LA. The result is a highly compact LiRA design with a substantially lower total weight. The second important advantage is that this design can be made symmetric, thereby eliminating the undesired tilting torque M_{tilt}. In fact, in the middle part of the piston, it is possible to place the rotary PMs symmetrically around the lateral surface.

Considering the limitations in space seen in Fig. 2, the PMs are finally placed as shown in Fig. 4(a), i.e., only at four equally spaced locations around the circumference of the piston. The PM segment at location A is the most constrained and can only span an angle of $\alpha_{PM,1} = 45°$. The maximum axial

length that can be fitted there sets the axial length of the rotor and is limited to $l_{\mathrm{PM}} = 5$ mm. The PM segment at location B, instead, can only span an angle of $\alpha_{\mathrm{PM},2} = 25°$. The PM segments at locations C and D are symmetric with respect to the z-axis to the ones at locations A and B, respectively. As a consequence of the PM locations, the rotary stators are placed as shown in Fig. 4(b). As can be noticed, most of each rotary stator is integrated into the stator extensions of the LA. To cover also the rotary magnets during the whole linear motion (and prevent unwanted axial reluctance forces), the total length of the rotary stator is $l_{\mathrm{stat,RA}} = z_{\mathrm{strk}} + l_{\mathrm{PM}} = 12$ mm. Note that owing to the presence of the pump's inlets and outlets, the stator cannot occupy the full circumference. As shown in Fig. 4(b), the angle spanned by the stator is limited to $\alpha_{\mathrm{stat,max}} = 110°$ on each side of the *ShuttlePump*.

B. PMSM TOPOLOGY SELECTION

In order to make the integration with the LA possible, only PMSM topologies with a slotted stator and a concentrated winding are considered for the RA. In fact, the main role of the stator extensions (and the pole shoes) used in the LA is to maintain approximately constant the total equivalent reluctance seen by the PMs of the translator while the piston shuttles along the axial direction. Without them, a strong axial reluctance pull force would appear as soon as the translator is displaced away from the center of the LA, which would compromise its operation [17]. With a slotted stator design, the RA can be integrated into the stator extensions of the LA, preserving its original air gap length $d_{\mathrm{gap}} = 1.5$ mm. Furthermore, in order to ensure that the overall reluctance profile is unchanged, pole shoes with large coverage and sufficient thickness have to be used. For what concerns the use of a concentrated winding, it is easily understood that it would greatly simplify the realization of the RA and its coils, as well as their interconnection with minimum wire length [23].

Based on these premises, it is possible to select the pole–slot combination of the RA according to the proposed placement of the stator and the PMs in Figs. 3(b) and 4. Three criteria guide the selection. First, given that the stator is, in fact, split into two halves, it is reasonable to choose an even number of slots N_{s}. Second, N_{s} should not be too high in order to ensure that all the parts of the stator (teeth, pole shoes, and coils) are easy to manufacture and assemble. Third, it is necessary to accommodate the same number of coils per phase, in order to guarantee that the inverter supplying the RA is loaded symmetrically. As a result, the most suitable combination is $N_{\mathrm{s}} = 12$ slots and $N_{\mathrm{p}} = 8$ poles. If the defined space constraints are also considered, the standard PMSM topology has to be substantially modified, as shown in Fig. 5(a). In particular, the dashed contours indicate the eliminated parts, i.e., two stator sectors, as well as most of the PMs. Consequently, it can be said that the RA module consists of two identical half-machines with $N_{\mathrm{s}} = 3$ slots and $N_{\mathrm{p}} = 2$ poles. Each half-stator covers an angle $\alpha_{\mathrm{stat}} = 90°$ and has one coil per phase, each concentrated around a stator tooth. Motors with partial stator coverage do exist in the literature for highly

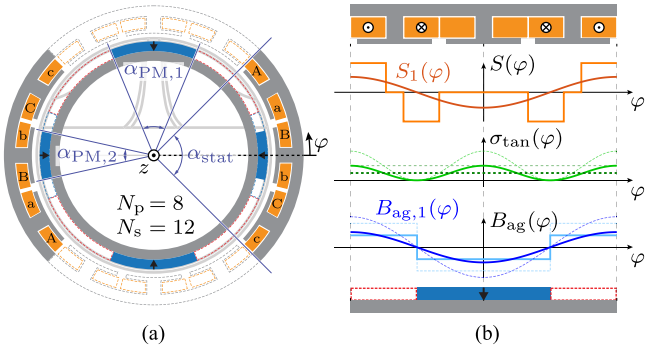

FIGURE 5. **(a) Proposed PMSM topology for the RA. The standard eight-pole 12-slot machine is specially adapted to the space constraints of the *ShuttlePump*, with the dashed contours indicating the eliminated parts. The result is two half-stators with three slots each and a rotor equipped with four magnet segments of only one polarity. (b) Exemplary machine plan (one half-stator) demonstrating that tangential force (and hence torque) generation is still possible even if part of the PMs is removed. $S(\varphi)$ is the current sheet with its fundamental component $S_1(\varphi)$, $\sigma_{\tan}(\varphi)$ is the area-related force density, and $B_{\mathrm{ag}}(\varphi)$ is the air gap magnetic flux density with its fundamental component $B_{\mathrm{ag},1}(\varphi)$. The dashed curves correspond to the standard PMSM topology, i.e., with full PM coverage.**

spatially constrained applications [24], [25], [26]. The PMs on the rotor will all have the same (radial) magnetization direction and polarity. Although the PMs of opposite polarity are suppressed, it can be shown that force generation is still possible (similarly, e.g., to consequent-pole machines [27], [28]), e.g., by inspecting the half-machine plan of Fig. 5(b). Furthermore, it is decided to use PMs of opposite magnetization with respect to the adjacent ones of the LA. As a consequence, one RA module will have only positively r-magnetized PMs ("north") and the other module only negatively r-magnetized ones ("south") [cf. Fig. 6(a)]. This way, the spatial periodicity of the magnetic field distribution along the axial direction is respected. This measure can potentially increase the generated axial force due to the interaction between the rotary PMs and the stator of the LA. Finally, it is ensured that at least a 1- or 2-mm-thick layer of core material is present in the region around the inlets and outlets that cannot be occupied by the rotary stator. These stator connectors are necessary to prevent an otherwise prohibitively strong cogging torque. However, as visible in Fig. 6(a), they need to have round notches (15-mm diameter) in correspondence with the inlets and outlets locations. As will be seen in Section IV-D and Fig. 12(a), this inevitably introduces a certain cogging torque component whenever the PMs are facing the notches during linear–rotary motion.

C. MAIN RA DESIGN AND INTEGRATION ASPECTS

In order to guarantee that the proposed RA concept can work correctly and meet the design specifications, there are a couple of important aspects that need to be considered.

As the rotor is only partly and irregularly equipped with PMs, a pronounced torque ripple ΔM_{ax} has to be expected. Two main components can be distinguished. One is the typical

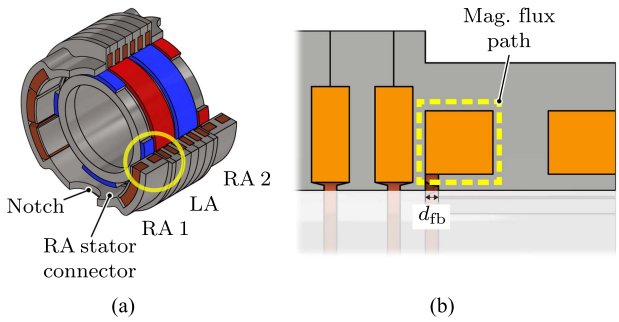

FIGURE 6. **(a) 3-D view of the proposed RA concept and topology in the context of the full LiRA. The two RA modules use PMs of opposite polarity with respect to the adjacent ones of the LA. The two half-stators of each RA module are connected by two arc segments made of core material in order to prevent strong cogging effects. Owing to the pump's inlets/outlets, these stator connectors need to be carved with round (Ø 15 mm) notches (4 in total). (b) Detailed cross-sectional view of the junction between the LA and an RA module, where a potential low-reluctance magnetic flux path can be formed. This can be avoided by introducing a flux barrier with length f_{fb}.**

cogging due to the interaction between the PMs and the two half stators, according to the geometry of their teeth and pole shoes. The other one, as mentioned, is introduced by the inlet/outlet notches on the stator connectors during linear–rotary motion. ΔM_{ax} has to be checked, as it causes a certain angular speed ripple $\Delta\Omega$. The transfer between ΔM_{ax} and $\Delta\Omega$ (in r/min) can be very simply modeled in the Laplace domain as the first-order low pass

$$\Delta\Omega(s) = \frac{(60/2\pi)}{s \cdot J_{mov}} \Delta M_{ax}(s) \tag{1}$$

where s is the Laplace variable and J_{mov} is the moment of inertia of the complete mover. This implies that, according to the value of J_{mov}, ΔM_{ax} can be significantly attenuated. For instance, consider a torque ripple fundamental $\Delta M_{ax,1} = M_{req} \sin(2\pi f_{rip} t)$, i.e., with an amplitude equal to 100% of the required axial torque $M_{req} = 3.1$ mN·m. Furthermore, recall that $\Delta M_{ax,1}$ exhibits $N_{cogg} = \text{lcm}(N_s, N_p) = 12$ periods per one revolution, and hence, $f_{rip} = 12\, f_{op}$. Already by solely considering the translator mass $m_{mov} = 130$ g of the previously designed LA to calculate J_{mov}, the largest angular speed ripple is obtained for $f_{op,min} = 1.5$ Hz, and its amplitude is

$$\Delta\hat{\Omega}_1 = \frac{(60/2\pi)}{2\pi\,(12 \cdot f_{op,min}) \cdot J_{mov}} M_{req} = 4.59 \text{ r/min} \tag{2}$$

which corresponds to only $\Delta\Omega_{\%} = \Delta\hat{\Omega}_1/\Omega_{op,min} = 0.051 = 5.1\%$ of the operational speed $\Omega_{op,min} = 90$ r/min. Therefore, even a pronounced torque ripple can be tolerated by the RA without compromising its operation, specially at higher angular speeds. It is then sufficient to ensure that the chosen machine design does not violate the angular speed ripple specification in Table 1 for $f_{op,min} = 1.5$ Hz. In addition, it should be considered that (2) is an open-loop calculation, but, in practice, the RA is operated in closed loop with an angular speed controller. Depending on the chosen control bandwidth, it can be shown that the ripple is attenuated even more. Finally, in order to set a design goal and simplify the subsequent FEM-based optimization, it is decided to neglect the ripple component introduced by the inlet/outlet notches and only consider the one caused by the interactions between the PMs and the stator teeth/pole shoes (easier to model in a 2-D FEM analysis). At the same time, the maximum allowed percent speed ripple is reduced to $\Delta\Omega_{\%,max} = 5\%$. This way, the RA is designed for very low torque ripple in the best case for which the stator notches have no influence. In practice, it is expected that the total torque ripple will be higher but tolerable, as argued. It is important at this point to highlight the main tradeoff in the RA design. The torque ripple ΔM_{ax} is mainly caused by reluctance forces, which, as such, depend quadratically on the air gap flux density B_{ag}. Therefore, ΔM_{ax} can be mitigated by reducing B_{ag} (e.g., using weaker/thinner PMs or larger air gap lengths). Conversely, for torque generation, we have

$$M_{in}(\varphi) \propto \sigma_{tan}(\varphi) = B_{ag,1}(\varphi) \cdot S_1(\varphi) \propto B_{ag}(\varphi) \cdot I_R \tag{3}$$

i.e., B_{ag} contributes directly, together with the equivalent current sheet $S(\varphi)$, to the (tangential) area-related force density $\sigma_{tan}(\varphi)$ [cf. Fig. 5(b)]. Therefore, to generate the same torque M_{in} with the least current I_R (and hence ohmic losses), B_{ag} should be large. This translates into the main design tradeoff, i.e., between angular speed ripple $\Delta\Omega$ and ohmic losses P_{Cu}.

Another crucial aspect is the interaction between the RA and the LA. In particular, it has to be verified that the two RA modules in tandem can continuously provide the required torque M_{req}, also if the linear motion of the piston is considered. Furthermore, it has to be ensured that the axial reluctance profile of the LA is truly unaffected by the integration of the RA. Moreover, as the RA is integrated just adjacent to the LA, it must be guaranteed that both their magnetic designs are not compromised. For instance, no magnetic flux path should be created between the two (RA and LA) stators instead of through the air gap and the respective rotor/translator. With the chosen topology, a critical location is the one shown in the detailed view of Fig. 6(b). If the bottom side of the pole shoes is in direct contact with the adjacent LA, a low-reluctance magnetic flux path through the two stators could be created. In order not to compromise torque generation, the inner side of the pole shoes is shortened, thus introducing a flux barrier with length d_{fb}.

One last aspect to consider concerns the total power losses, which need to be kept below the specified loss budget of $P_{Cu,RA,max} = 0.5$ W. Owing to the low operational frequencies f_{op}, ac losses can be neglected, and hence, the dominant loss component is ohmic. This can be sensibly reduced if the cross section of the RA coils is as large as possible. It is also important to consider beforehand practical aspects of the RA realization, such as manufacturing tolerances introducing potential unwanted air gaps or realistic reluctances along the main magnetic paths of the machine due to the used magnetic material [29], [30]. As will be discussed in Section V-C, they cause a reduction of the magnetic flux with respect to the

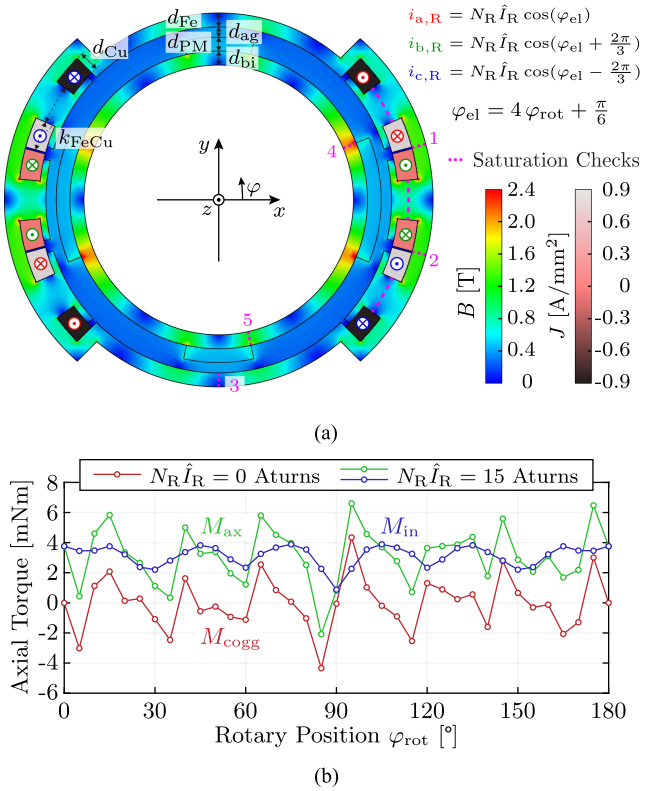

FIGURE 7. **(a) 2-D FEM Cartesian model of the RA for an exemplary design, with indicated parameters and solved *B* and *J* fields (*Ansys Maxwell*). (b) Exemplary axial torque profiles for the cases $N_R\hat{I}_R = 15$ Aturns, giving the total axial drive torque $M_{ax}(\varphi_{rot})$ and $N_R\hat{I}_R = 0$ Aturns, giving the cogging torque component $M_{cogg}(\varphi_{rot})$. Their difference is the generated torque $M_{in}(\varphi_{rot})$.**

predicted/simulated values, with a consequent increase in the required current and hence ohmic losses, to generate the same torque. In order to account for these additional components, the targeted ohmic losses for the following FEM-based optimization are $P_{Cu,RA} = 0.1$ W at most.

IV. FEM MACHINE OPTIMIZATION

This section discusses the validation and optimization of the proposed RA concept by means of parameterized 2-D and 3-D FEM models. For a given RA design providing the required average torque $M_{req} = 3.1$ mN·m, the optimization outputs to consider are the torque (and hence speed) ripple and the ohmic losses. In addition, the resulting rotor mass is included. The optimization is conducted in 2-D. Then, the interactions of the selected design with the LA are investigated in a 3-D analysis.

A. 2-D FEM MODEL OF THE RA

The 2-D Cartesian FEM model includes the parameterized cross section of one of the RA modules, as shown in Fig. 7(a). The model parameters are summarized in Table 2. Owing to the low operational frequencies, the model can be solved for magnetostatic conditions, which require less computational effort but neglect ac effects. As the arcs spanned by a tooth and a coil add up to a stator slot pitch, only one parameter

TABLE 2 **Parameters of the FEM Models**

Name	Symbol	Value	Unit
Relative permeability (core)	μ_r	4000	
Mag. saturation threshold (core)	B_{sat}	2.2	T
Copper conductivity (with fill factor)	$\sigma_{Cu,ff}$	3.4	MS/m
Fill factor	k_{ff}	0.6	
PM coercitivity	H_c	1000	kA/m
Relative permeability (PM)	μ_{PM}	1	
Active machine length	l_{PM}	5	mm
Pole shoe coverage	k_{shoe}	0.8	
PM angle (large segment)	$\alpha_{PM,1}$	45	°
PM angle (small segment)	$\alpha_{PM,2}$	25	°
Magnetic gap length	d_{ag}	Opt	mm
PM thickness	d_{PM}	Opt	mm
Copper layer thickness	d_{Cu}	Opt	mm
Iron-copper ratio	k_{FeCu}	Opt	
Stator core thickness	d_{Fe}	Opt	mm
Back iron thickness	d_{bi}	Opt	mm
Axial stroke length (3D model)	z_{strk}	8	mm
Flux barrier length (3D model)	d_{fb}	Opt	mm
Average torque output	M_{req}	3.1	mNm
Max. angular speed ripple	$\Delta\Omega_{\%,max}$	5	%
Loss budget	$P_{Cu,RA,max}$	0.5	W

k_{FeCu} (iron-to-copper ratio) is introduced. Furthermore, the pole shoe coverage is defined by the parameter k_{shoe}, with $k_{shoe} = 1$ indicating a fully closed slot. The modeled materials have simplified definitions. For the stator core and the rotor back iron, a linear ferromagnetic material with $\mu_r = 4000$ and negligible conductivity is used. It is then necessary to check for potential magnetic saturations after the model is solved, ensuring that the B field is below a specified limit (e.g., 1.6 T for electrical steel). The coils are modeled with solid copper cross sections, i.e., with a single turn. A realistic fill factor of $k_{ff} = 0.6$ is considered by modeling the copper material with a reduced conductivity $\sigma_{Cu,ff} = k_{ff}\,\sigma_{Cu} = 3.4$ MS·m^{-1}. Finally, the PMs are modeled with a coercivity $H_c = 1000$ kA·m^{-1}, which approximately corresponds to the N50 magnetization grade of commercial NdFeB PMs. The magnetization direction is radial. The three phase currents are assigned to the coils, as indicated in Fig. 7(a). The assignment yields maximum torque per ampere using field-oriented control with the electrical angle φ_{el}.

The main simulation outputs are the torque profile $M_{ax}(\varphi_{rot})$ and the ohmic losses P_{Cu}. The 2-D Cartesian model returns the torque per 1 m of length along the z-direction, so it is scaled by multiplying by the active length $l_{PM} = 5$ mm. The total torque profile $M_{ax}(\varphi_{rot})$ obtained for an exemplary design with a test current $N_R\hat{I}_R = 15$ Aturns is shown in Fig. 7(b). It is the sum of two components, namely, the generated (internal) torque $M_{in}(\varphi_{rot})$ and the cogging torque $M_{cogg}(\varphi_{rot})$. As can be noticed, the total torque ripple $\Delta M_{ax}(\varphi_{rot})$ does not just correspond to the cogging torque $M_{cogg}(\varphi_{rot})$, but also the internal torque $M_{in}(\varphi_{rot})$ contributes to it. The ohmic losses P_{Cu} are also returned per 1 m of machine length along the z-direction. In this case, the used scaling length is not just the active length l_{PM} but the average coil length $l_{coil,avg}$. This also considers the two sides of the coil serving as return conductors and not contributing to torque generation. The resulting ohmic

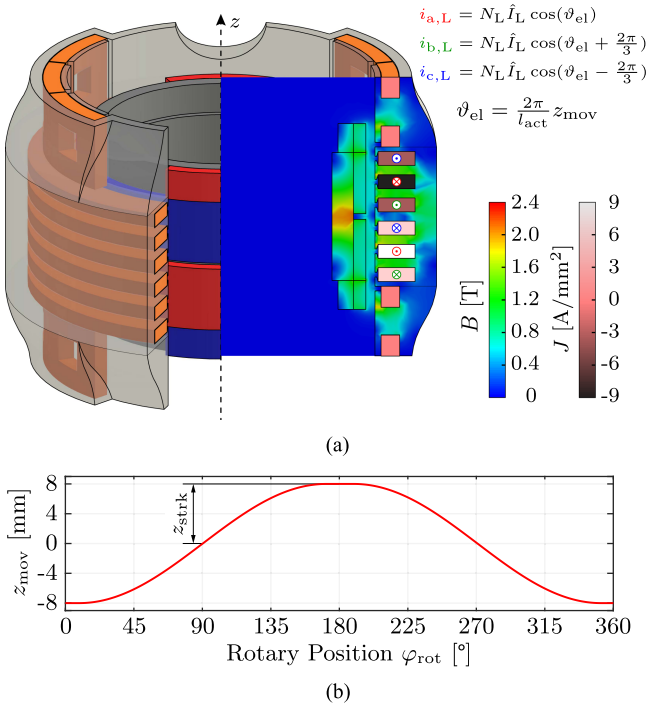

FIGURE 8. (a) 3-D FEM model of the LiRA with exemplary *B* and *J* fields on the *xz*-section. The currents $i_{\{a,b,c\},L}$ are impressed in the winding of the LA to generate maximum force per ampere with the (linear) electrical angle ϑ_{el} [17]. (b) Linear–rotary motion profile of the *ShuttlePump*, assigned to the mover of the 3-D FEM model. The linear motion follows a quasi-sinusoidal trajectory, with a stroke length $z_{strk} = 8$ mm [16].

losses are valid for one RA module. Finally, the returned values of the B field used to check for magnetic saturations in the stator also have to be scaled. This is because the 2-D model assumes that the geometry extends unchanged along the z-axis, i.e., rotor, pole shoes, and teeth have the same length, which is not the case in practice. The scaling factor is the ratio of the tooth length l_{tooth} over the active length l_{PM}.

B. 3-D FEM MODEL OF THE FULL LIRA

A 3-D FEM model of the full LiRA is needed to check the possible interactions between the RA and the LA during the combined linear–rotary motion of the piston. Furthermore, it allows estimating the total torque ripple ΔM_{ax} also considering the effect of the round inlet/outlet notches that need to be made on the rotary stators [cf. Fig. 6(a)]. Another important detail that can only be modeled and investigated in 3-D is the length of the flux barrier d_{fb} between the pole shoes of the RA and the stator of the LA, introduced in Fig. 6(b). The model is shown in Fig. 8(a). The LA part is compatible with the geometry and dimensions of the realized LA and is adapted from existing 3-D models used for its analysis [17]. The RA part is parameterized analogously to its 2-D counterpart. The linear–rotary position of the mover is parameterized according to the required piston motion profile of the *ShuttlePump* [16], as reported in Fig. 8(b). The simulation returns, besides the total copper losses $P_{Cu,tot}$, also the overall profile of the axial force $F_{ax}(\varphi_{rot}, z_{mov})$ and the total torque $M_{ax,tot}(\varphi_{rot}, z_{mov}) = M_{ax,1}(\varphi_{rot}, z_{mov}) + M_{ax,2}(\varphi_{rot}, z_{mov})$ provided by the two RA modules operating together.

TABLE 3 Swept Optimization Parameters

Name	Symbol	Range	Step	Unit
Group 1 (Main)				
Magnetic gap length	d_{ag}	[1, ..., 2]	0.5	mm
PM thickness	d_{PM}	[1, ..., 3, 5]	0.5	mm
Copper layer thickness	d_{Cu}	[2, ..., 6]	1	mm
Iron-copper ratio	k_{FeCu}	[0.2, ..., 0.8]	0.2	
Group 2				
Stator core thickness	d_{Fe}	[2, ..., 4]	0.5	mm
Back iron thickness	d_{bi}	[2, ..., 4]	0.5	mm

C. RA OPTIMIZATION PROCEDURE

The optimization of the RA is conducted on the 2-D FEM model, due to the considerably higher computational effort needed to solve the 3-D model repeatedly. Nevertheless, the 2-D solutions provide all the necessary information to compare the RA designs together. The optimization procedure consists of three steps.

1) PRELIMINARY (COVERAGE)

Some parameters can already be fixed beforehand, thus reducing the number of designs to simulate in the 2-D FEM. Besides the angles spanned by the PMs, which, as seen, are maximized to $\alpha_{PM,1} = 45°$ and $\alpha_{PM,2} = 25°$, the parameters of the pole shoes can also be fixed. Owing to manufacturing constraints, their thickness is selected to be $d_{shoe} = 1$ mm. The shoe coverage, determined by the parameter k_{shoe}, should be as large as possible for two reasons. First, it contributes to reducing the amplitude of the cogging torque of the RA. Second, it is necessary to keep the reluctance seen by the PMs of the LA approximately constant along the axial direction. In order to prevent fringing effects, $k_{shoe} = 0.8$ is selected.

2) MAIN (EXPLORATION)

The parameters that are instead swept are listed in Table 3. In the main optimization step, the parameters of Group 1 are varied. These parameters are expected to have the most influence on the machine design. In fact, they include both magnetic parameters (d_{ag}, d_{PM}, and k_{FeCu}) that directly influence the air gap flux density B_{ag} and copper-related parameters (d_{Cu} and k_{FeCu}), which determine the cross section of the stator coils $A_{Cu,0}$ and, hence, have a direct impact on the ohmic losses P_{Cu}. The design space obtained with the $3 \times 6 \times 5 \times 4 = 360$ parameter configurations is visualized in Fig. 9 on the P_{Cu}–$\Delta\Omega_{\%}$ plane. For each design, a (total) torque profile such as the one in Fig. 7(b) is simulated, from which the average $M_{ax,avg}$ and ripple $\Delta M_{ax}(\varphi_{rot})$ are considered.

It should be noticed that for the proposed topology, the ripple on the internal (and hence total) torque depends on the amplitude of the current $N_R \hat{I}_R$. For this reason, each design is initially simulated with a test current $N_R \hat{I}_{R,test} = 30$ Aturns, which allows determining the scaling factor $k_{scal} =$

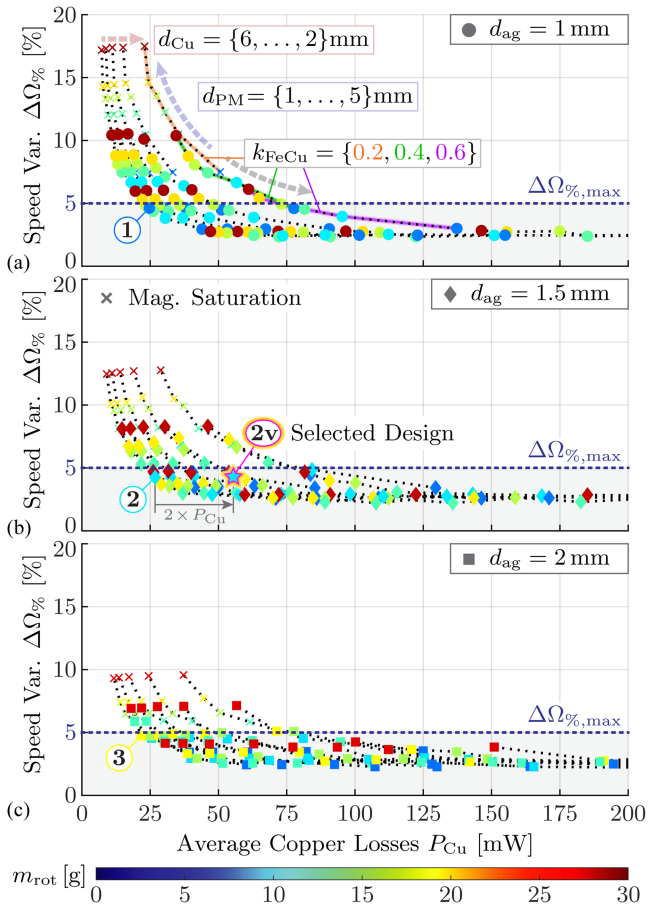

FIGURE 9. Design space generated by the second optimization step, visualized on the P_{Cu}–$\Delta\Omega_{\%}$ for (a) $d_{ag} = 1$ mm, (b) $d_{ag} = 1.5$ mm and (c) $d_{ag} = 2$ mm. The color of each point indicates the rotor mass m_{rot}. The points with the same parameters' configuration except for d_{PM} are connected by dashed lines. This way, the effect of the remaining swept parameters is visible, as indicated in (a). The considered threshold for magnetic saturation is $B_{sat} = 2.2$ T. The limit in speed variation is reported, which allows the identification of the feasible designs.

$M_{req}/M_{ax,test}$, where $M_{ax,test}$ is the average total torque obtained for the test current $N_R\hat{I}_{R,test}$. By adjusting the current amplitude to $N_R\hat{I}_{R,req} = k_{scal}\,N_R\hat{I}_{R,test}$, all the designs are simulated for the same average torque output $M_{req} = 3.1$ mN·m and with the correct total torque ripple $\Delta M_{ax}(\varphi_{rot})$, ensuring a fair comparison. From $\Delta M_{ax}(\varphi_{rot})$ thus simulated, the speed ripple $\Delta\Omega$ is calculated according to the low-pass dynamics in (1) for the worst case scenario, i.e., $f_{op,min} = 1.5$ Hz and expressed as a percent of the rotational speed $\Omega_{op,min}$. Finally, the single-turn average coil length $l_{coil,avg}$ (used to scale the ohmic losses P_{Cu}), as well as the mass of the rotor m_{rot} and hence the moment of inertia of the mover J_{mov}, are also specifically calculated for each design. In Fig. 9(a)–(c), the results are grouped according to the value of d_{ag} in order to better visualize the effect of the remaining optimization parameters. As expected, a larger air gap length d_{ag} yields a smaller air gap flux density B_{ag}, which reduces the cogging torque but increases the ohmic losses, with the consequence that (for a constant output torque) the group of designs moves along a hyperbolic front on the P_{Cu}–$\Delta\Omega_{\%}$ plane [cf. (3)]. This can be analogously seen for different values of d_{PM}, considering, e.g., a group of designs connected by a dashed line. Both parameters influence the equivalent air gap reluctance (as the magnetic permeability of the PMs $\mu_{PM} \approx \mu_0$), but d_{PM} also defines the magnetomotive force provided by the PMs. The parameter d_{Cu} does not have a pronounced effect on $\Delta\Omega_{\%}$, but solely on P_{Cu}. This is expected, as d_{Cu} defines the available coil cross section $A_{Cu,0}$ but does not influence the air gap flux density B_{ag}. In Fig. 9(a)–(c), one can observe how a group of designs scales along the P_{Cu}-axis according to the value of d_{Cu}. Therefore, for minimum ohmic losses, d_{Cu} should be increased as far as possible, fully utilizing the maximum allowed outer diameter (but also considering the thickness of the stator core d_{Fe}). The parameter k_{FeCu} affects instead both $\Delta\Omega_{\%}$ and P_{Cu} directly. In fact, by defining the thickness of the stator teeth, it still determines $A_{Cu,0}$, but it additionally affects the circumferential air gap reluctance profile. A large value of k_{FeCu} gives a smoother air gap reluctance profile, which translates into reduced cogging torque (and hence $\Delta\Omega_{\%}$). However, this way, the copper cross section $A_{Cu,0}$ is also reduced, with an overall increase in P_{Cu}. As a result, the choice of k_{FeCu} is not obvious, thus providing further motivation to conduct the FEM-based optimization.

TABLE 4 Feasible RA Designs Under the Specified Constraints

#	d_{ag}	d_{PM}	d_{Cu}	k_{FeCu}	$\Delta\Omega_{\%}$	P_{Cu}	m_{rot}
1)	1 mm	1 mm	6 mm	0.6	4.6 %	25 mW	7.4 g
2)	1.5 mm	1.5 mm	6 mm	0.4	4.2 %	27 mW	10 g
2v)	1.5 mm	1.5 mm	3 mm	0.4	4.3 %	55 mW	10 g
3)	2 mm	3 mm	6 mm	0.4	4.7 %	22 mW	19 g

The main constraint of $\Delta\Omega_{\%,max} = 5\%$ defines the subset of feasible designs. Among these, four relevant ones are selected and reported in Table 4. *Design 3* is the one attaining the least losses, but it needs relatively thick PMs, resulting in the heaviest rotor. Therefore, at the cost of slightly higher losses, *Design 1* or *Design 2* shall be preferred. *Design 2* has the practical advantage of having the same air gap length $d_{ag} = 1.5$ mm as the designed LA, so the complete mover can have the same outer diameter. Furthermore, as the resulting values of P_{Cu} are way within the losses budget $P_{Cu,RA,max} = 0.5$ W (i.e., very small compared to the losses of the LA), it is decided to halve the coil thickness at the cost of doubling the ohmic losses, which corresponds to *Design 2v* [cf. Fig. 9(b)]. The important advantage is the overall rounder form factor of the LiRA, which facilitates implantation considerably. A final estimation of the total losses of the RA is provided in the next subsection, as it requires the total torque profile with both RA modules operating together, obtained from the 3-D simulations.

3) AVOID SATURATION

As a last step, the parameters of Group 2 are swept for the selected design, i.e., the thickness of the stator core d_{Fe} and

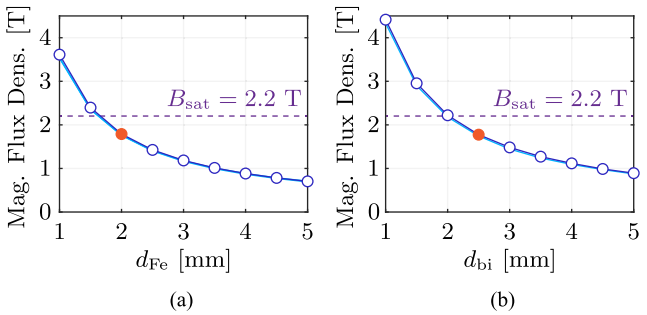

FIGURE 10. Results of the third optimization step. (a) Average magnetic flux density at the locations 1–3 in the stator core indicated in Fig. 7(a) versus the thickness d_{Fe}. (b) Average magnetic flux density at the locations 4 and 5 in the rotor back iron indicated in Fig. 7(a) versus the thickness d_{bi}.

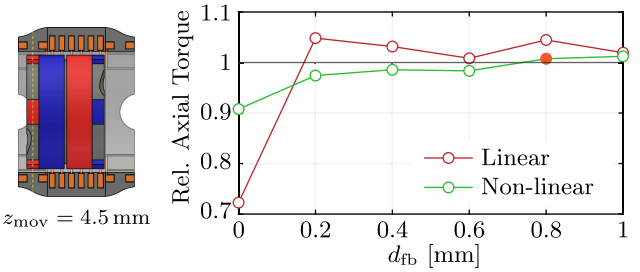

FIGURE 11. Effect of the flux barrier at the interface between LA and RA [cf. Fig. 6(b)]. The simulated average torque is obtained for the two cases of linear ($\mu_r = 4000$) and nonlinear (*VACOFLUX50*) material definitions for the stator cores and mover back iron. For the selected LiRA design, due to the thin pole shoes, the torque reduction without a flux barrier is not critical.

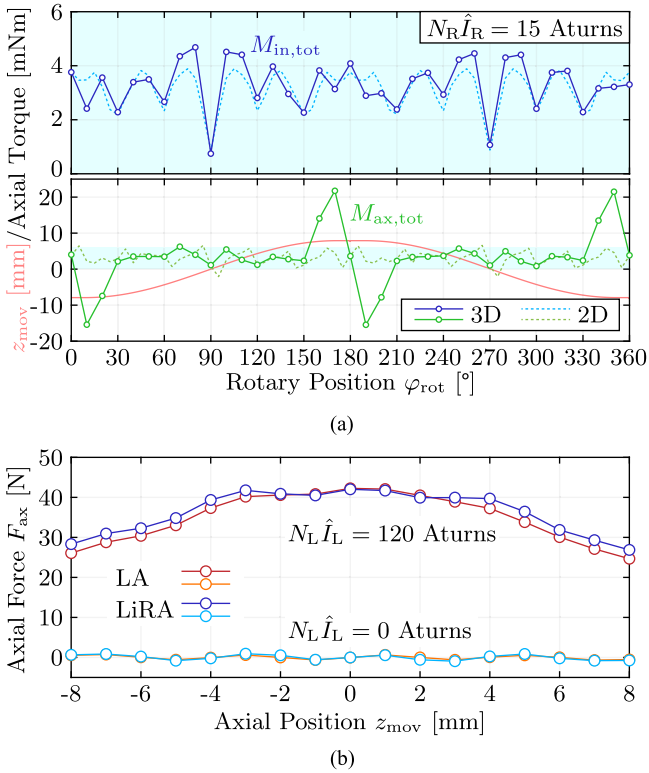

FIGURE 12. Results of the 3-D FEM simulations of the complete LiRA. (a) Internal and total axial torques $M_{in,tot}(\varphi_{rot})$ (zoomed range) and $M_{ax,tot}(\varphi_{rot})$ applied to the mover by both the RA modules operating together, compared to their 2-D counterparts. The mover follows the specified linear–rotary motion profile, reported in light red from Fig. 8(b). (b) Axial force profile $F_{ax}(z_{mov})$ for the cases $N_R\hat{I}_R = N_L\hat{I}_L = 0$ Aturns (unenergized LiRA, giving the axial cogging force profile) and $N_L\hat{I}_L = 120$ Aturns, $N_R\hat{I}_R = 15$ Aturns (energized LiRA, giving the axial drive force profile). Both the cases are compared to the results of the original LA design [17], verifying that the cogging force is almost unchanged, and the force generation is even slightly improved.

of the rotor back iron d_{bi} are optimized. In particular, both parameters should be minimized for a compact and lightweight design, but it must be ensured that no saturation of the magnetic material occurs. Fig. 10(a) and (b) reports the simulated average magnetic flux densities in the stator core and the rotor back iron versus d_{Fe} and d_{bi}, respectively. For each location 1–5 in Fig. 7(a), this is calculated over all rotary positions, and only the curve with the largest values is considered. With the threshold $B_{sat} = 2.2$ T for *VACOFLUX50*, $d_{Fe} = 2$ mm and $d_{bi} = 2.5$ mm are selected.

D. INTEGRATION AND INTERACTIONS WITH THE LA

Once the 2-D optimization is finalized, the selected RA design is investigated in 3-D to verify its interactions with the adjacent LA. First, the length of the flux barrier d_{fb} highlighted in Fig. 6(b) has to be chosen. Fig. 11 shows the results of a series of 3-D simulations with the average axial torque obtained for different values of d_{fb} ranging from 0 to 1 mm. For a more direct comparison with the 2-D counterpart, the simulations are conducted for a fixed $z_{mov} = 4.5$ mm (i.e., with one of the rotors directly facing the RA stator teeth) and the same RA current $N_R\hat{I}_{R,req} = 15$ Aturns. The average torque is then normalized to $M_{req} = 3.1$ mN·m. Furthermore, both linear and nonlinear material definitions for the stator core and rotor back iron are used. The results indicate that the absence of a flux barrier at the interface between LA and RA would be a concern in principle, but does not have a major impact on torque generation for the chosen design. With the linear material definition, for $d_{fb} = 0$, the generated torque is about 30% weaker, and, as expected, it gets to the nominal value (and even slightly above) as soon as the flux barrier is introduced. With the more realistic nonlinear material definition for *VACOFLUX50*, this effect is less pronounced. This can be explained by the fact that the geometry of the pole shoe, specially due to its thickness $d_{shoe} = 1$ mm, is already offering high reluctance along the considered critical flux path. Finally, $d_{fb} = 0.8$ mm is selected.

The results of the 3-D simulations of the complete LiRA with the piston following the linear–rotary motion profile of Fig. 8(b) are reported in Fig. 12. For these simulations, only the nonlinear material definition for the stator cores and mover back iron is used. In Fig. 12(a), the internal torque $M_{in,tot}(\varphi_{rot})$

and the total torque $M_{\mathrm{ax,tot}}(\varphi_{\mathrm{rot}})$ provided by both RA modules are reported and compared to their 2-D counterparts. From $M_{\mathrm{ax,tot}}(\varphi_{\mathrm{rot}})$, it is possible to observe the expected cogging torque component introduced by the inlet/outlet notches on the rotary stators. In fact, there are two doublets of opposite torque peaks right around the two rotary positions $\varphi_{\mathrm{rot}} = 0°$ and $\varphi_{\mathrm{rot}} = 180°$. As can be understood from the linear motion profile [$z_{\mathrm{mov}}(\varphi_{\mathrm{rot}})$, reported from Fig. 8(b)], those are the two conditions for which the mover reaches one of the two axial edges of the LiRA and, hence, the rotary PMs move in front of the notches. The additional cogging torque increases the percent speed ripple to $\Delta\Omega_{\%} = 14\,\%$, which, however, remains within the allowed range. Importantly, on average, the total internal torque is still $M_{\mathrm{in,tot,avg}} = 3.1\ \mathrm{mN{\cdot}m}$. As visible from the internal torque profiles [compared in the zoomed range of Fig. 12(a)], during the linear–rotary motion of the mover, both the RA modules contribute to maintaining approximately the same internal torque profile as if only one module were acting on a single rotor. However, this also means that the required ohmic losses will be approximately doubled. The 3-D simulation returns in fact $P_{\mathrm{Cu,tot}} = 6\,R_0\,(N_{\mathrm{R}}\hat{I}_{\mathrm{R}})^2 = 102\ \mathrm{mW}$. Fig. 12(b) shows instead the profile of the axial force $F_{\mathrm{ax}}(z_{\mathrm{mov}})$ acting on the mover. Two cases are considered, namely, when the LiRA is not energized and when it is, and compared to the corresponding results that are valid for the original design of the LA with its stator extensions [17]. In the first case, it is possible to verify that the axial reluctance profile of the original LA is maintained, and hence, no large axial cogging forces are introduced. In the second case, it can be observed that adding the RA modules not only does not impair axial force generation, but even improves it due to the chosen arrangement of the PMs of the RA. It can be calculated that this increase in the machine constant of the LA contributes to an overall reduction in ohmic losses with respect to the original design amounting to 4%.

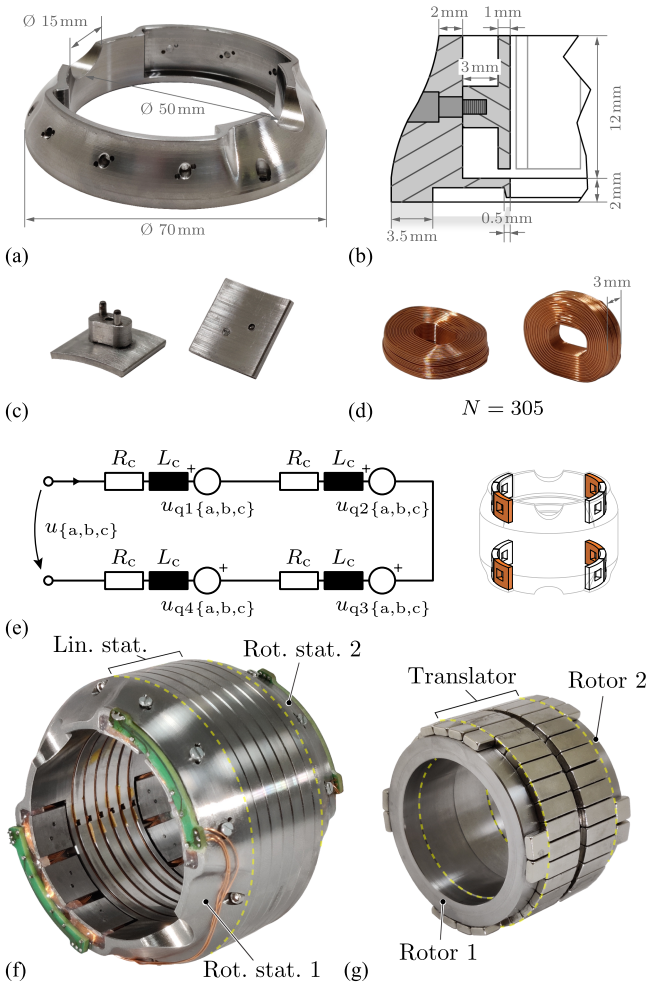

FIGURE 13. Realized hardware prototype of the RA. (a) Realized stator core made of *VACOFLUX50*. (b) Stator section at the coils side (*xz*-) with annotated dimensions. (c) Realized demountable stator teeth with large-coverage pole shoes. (d) Realized stator coil with a special bent shape, made of a 0.18 G1B coated copper wire with $N_{\mathrm{R}} = 305$ turns. (e) Interconnection diagram valid for each phase {*a*, *b*, *c*} of the RA, including the equivalent circuits of each stator coil with the resistance R_{c}, the inductance L_{c}, and the induced voltages $u_{\mathrm{q\{1,2,3,4\}\{a,b,c\}}}$. (f) Complete stator assembly equipped with coils, side interconnection PCBs and mounted together with the LA. (g) Realized complete mover with back iron rings and multiple NdFeB PMs. It consists of the previously realized translator of the LA plus the two rotors of the RA on the sides. The mover will be finally integrated into the piston [cf. Fig. 4(a)].

V. HARDWARE PROTOTYPE

This section describes the hardware prototype of the selected RA design and provides insight into a specific type of mechanical assembly tolerance. Furthermore, the test bench used for the experimental measurements is presented.

A. STATOR REALIZATION

1) STATOR CORE

The realized stator core is shown in Fig. 13(a). The material used is the same as for the LA, i.e., the *VACOFLUX50*. Owing to the low operational frequencies, the material is not laminated. As visible from the sectional view in Fig. 13(b), half of an LA stator ring is integrated as a single piece with the rotary stator core. This facilitates the manufacturing of the half-ring and ensures a solid buildup. Furthermore, the sectional view shows the solution chosen for the realization of the stator teeth and pole shoes, which ensures an easy mounting of the coils. As depicted in Fig. 13(c), each stator tooth with its large pole shoe is realized as a separate part, made up of two pieces glued together. This way, the tooth can be inserted through a single coil and screwed to the stator core. Two pins with a diameter of 1 mm are used to connect all the parts (pole shoe, tooth, and stator) together and align them correctly. All six coils can thus be held firmly in place.

2) COILS

As shown in Fig. 13(d), the coils are specially manufactured with a bent shape to maximize the fill factor k_{ff}. It is advantageous to select a large number of turns N_{R} so that smaller currents have to be supplied by the inverter, thus reducing its conduction losses. At the same time, N_{R} should not be

too large, as it can be difficult to precisely control the phase currents to very small values due to, e.g., noise on the current measurement signals. Furthermore, the induced voltages in each phase $u_{q,\{a,b,c\}}(t)$ also have to be taken into account in order to guarantee that the currents can be impressed until the maximum operational speed. In fact, the three-phase inverter module (*MP6535* by *Monolithic Power Supply*, already used to supply the LA [17]) can be operated with a maximum dc-link voltage of $U_{\mathrm{DC,lim}} = 26$ V, which gives $U_{\{a,b,c\},\mathrm{lim}} = U_{\mathrm{DC,lim}}/2 = 13$ V. The selected compromise value for the number of turns is $N_R = 305$ that can be fitted in the given cross section $A_{\mathrm{Cu},0}$ with a 0.18 G1B coated copper wire. The resulting fill factor is $k_{\mathrm{ff}} = 0.61$, and the inverter current amplitude for nominal torque is $\hat{I}_{\mathrm{inv}} = 49.2$ mA. The measured electrical characteristics of a manufactured coil, namely, the DC coil resistance and inductance, are $R_c = 6.4\ \Omega$ and $L_c = 6.9$ mH (mounted in the stator). The maximum induced voltage is checked, considering the maximum induced voltage per turn for each coil and their interconnection in the two RA modules. All the coils are energized at the same time and, hence, supplied by a single three-phase inverter module. Therefore, this is loaded with four coils in series per phase, as depicted in the interconnection diagram (equivalent circuit) of Fig. 13(e). The induced voltages per turn $u_{q,\{a,b,c\},1}(t)$ are found for each phase by taking the time derivatives of the single-turn flux linkages $\psi_{\{a,b,c\},1}(t)$ obtained from the 3-D FEM simulations. The maximum induced voltage found (over all phases) is $U_{\mathrm{q,max}} = 3.28$ V. Neglecting the voltage drop on the inductance L_c due to the low operating frequency $f_{\mathrm{op}} = 5$ Hz, the required phase voltages are $u_{\{a,b,c\}}(t) = 4\,R_c\,i_{\{a,b,c\},R}(t) + u_{q,\{a,b,c\}}(t)$, which is at most $U_{\mathrm{max}} = 4.35\ \mathrm{V} < U_{\{a,b,c\},\mathrm{lim}}$. For the final assembly, as shown in Fig. 13(f), the coils are fixed to the stator core, and their terminals are guided to small printed circuit boards (PCBs) placed on the outer side of the RA, in order to facilitate their interconnection.

B. ROTOR REALIZATION

Fig. 13(g) shows the complete mover to be embedded in the piston, i.e., the translator of the LA plus the two rotors of the RA at its two axial ends. Each rotor is very simply built using a back iron ring made of *VACOFLUX50* and small NdFeB PMs glued on the outer surface. Their thickness is the chosen $d_{\mathrm{PM}} = 1.5$ mm, and their magnetization grade is N48. According to the chosen RA concept, all the magnets of one rotor are oriented in the same direction (i.e., with their magnetization axis pointing radially inwards or outwards of it), whereas the magnets of the other rotor have opposite polarity. The weight of a single rotor is $m_{\mathrm{rot}} = 48$ g. Together with the mass of the translator of the LA $m_{\mathrm{mov}} = 148$ g, the total mover mass is $m_{\mathrm{tot}} = 244$ g.

C. EFFECT OF THE STATOR ASSEMBLY TOLERANCES

An important aspect to consider for the realized prototype is the effect of mechanical tolerances in the assembly of the RA stators [29], [30]. This can lead to a considerable reduction

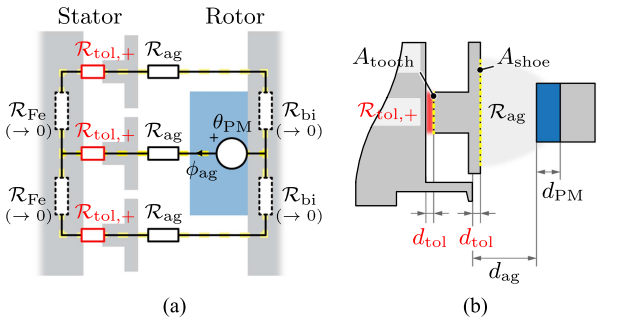

FIGURE 14. (a) Simplified equivalent magnetic circuit of the RA. The air gaps introduced between each tooth and the stator core due to tolerances in the stator assembly add the undesired reluctances $\mathcal{R}_{\mathrm{tol},+}$. The relative dimensions of the individual parts are intentionally not to scale. (b) Stator section with a protruding tooth. The reduction in the main air gap reluctance $\mathcal{R}_{\mathrm{ag}}$ does not compensate for the introduced $\mathcal{R}_{\mathrm{tol},+}$ due to the different equivalent cross sections of the flux path at the tooth side (A_{tooth}) and pole shoe side (A_{shoe}).

in the generated torque, which corresponds to an increase in the required ohmic losses. This is the reason why, in Section III-C, a rather conservative margin within the available losses budget (0.1 W out of the allowed $P_{\mathrm{Cu,RA,max}} = 0.5$ W) was defined for the RA optimization. The most critical manufacturing tolerances concern the mounting of the stator teeth to the rest of the stator core according to Fig. 13(b). In fact, if the two contact surfaces are not perfectly matched, at the interface between each tooth and the rest of the stator, a certain undesired air gap is introduced, to which the magnetic design of the RA results very sensitive. For a qualitative understanding, consider the magnetic circuit in Fig. 14(a), defined by the main magnetic flux paths in the RA. This is substantially simplified by assuming a planar homogeneous field in the radial direction and neglecting fringing effects. Furthermore, under the assumption $\mu_{\mathrm{PM}} \approx \mu_0$, the reluctance of the PM is included in the total air gap reluctance $\mathcal{R}_{\mathrm{ag}}$. Each undesired tolerance air gap with length d_{tol} (here assumed to be all equal for simplicity) adds a reluctance $\mathcal{R}_{\mathrm{tol},+} = \frac{d_{\mathrm{tol}}}{\mu_0 A_{\mathrm{tooth}}}$ to the magnetic circuit, where A_{tooth} is the equivalent cross section of the flux path at the back of the tooth. At the same time, as illustrated in Fig. 14(b), the total air gap length $d_{\mathrm{ag}} + d_{\mathrm{PM}}$ is reduced by d_{tol}. Therefore, the total air gap reluctance $\mathcal{R}_{\mathrm{ag}}$ is reduced by $\mathcal{R}_{\mathrm{tol},-} = \frac{d_{\mathrm{tol}}}{\mu_0 A_{\mathrm{shoe}}}$, where A_{shoe} is the equivalent cross section of the flux path in front of the pole shoe. If the equivalent cross sections A_{tooth} and A_{shoe} were the same, the total reluctance

$$\mathcal{R}_{\mathrm{ag,tot}} = 1.5\,(\mathcal{R}_{\mathrm{ag}} + \mathcal{R}_{\mathrm{tol},+} - \mathcal{R}_{\mathrm{tol},-}) \tag{4}$$

would be unchanged, as $\mathcal{R}_{\mathrm{tol},+} = \mathcal{R}_{\mathrm{tol},-}$ (note that the factor 1.5 is obtained considering the two parallel branches of the equivalent circuit). In that case, the magnetic design would be insensitive to the assembly tolerances of the stator teeth. Nevertheless, as $A_{\mathrm{tooth}} < A_{\mathrm{shoe}}$, then $\mathcal{R}_{\mathrm{tol},+} > \mathcal{R}_{\mathrm{tol},-}$, so the total reluctance $\mathcal{R}_{\mathrm{ag,tot}}$ can considerably increase. In more

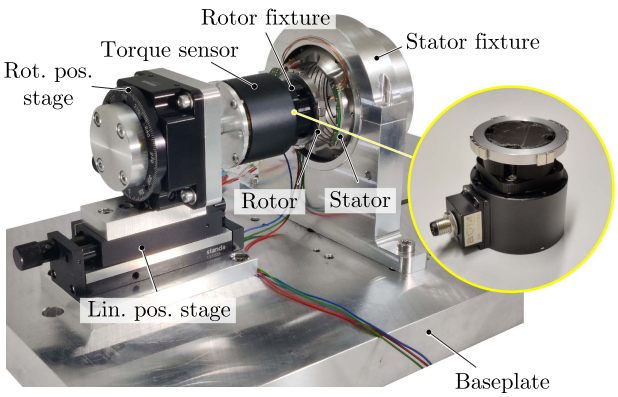

FIGURE 15. Experimental test bench used for the commissioning (torque measurement) of the RA. The close-up view shows how the single rotor is directly mounted to the sensor with a rigid plastic fixture.

detail, (4) can be written as

$$\mathcal{R}_{\mathrm{ag,tot}} = 1.5 \left(\frac{d_{\mathrm{g}} + d_{\mathrm{PM}}}{\mu_0 A_{\mathrm{shoe}}} + \frac{d_{\mathrm{tol}}}{\mu_0 A_{\mathrm{tooth}}} - \frac{d_{\mathrm{tol}}}{\mu_0 A_{\mathrm{shoe}}} \right). \quad (5)$$

By introducing the ratio $k_{\mathrm{A}} = A_{\mathrm{shoe}}/A_{\mathrm{tooth}}$, all the reluctances in (5) can be expressed with respect to A_{shoe}, obtaining

$$\mathcal{R}_{\mathrm{ag,eq}} = 1.5 \, \frac{d_{\mathrm{g}} + d_{\mathrm{PM}} + (k_{\mathrm{A}} - 1)\, d_{\mathrm{tol}}}{\mu_0 A_{\mathrm{shoe}}} \quad (6)$$

which shows that the equivalent air gap is increased by $(k_{\mathrm{A}} - 1)\, d_{\mathrm{tol}}$, i.e., that the contribution of d_{tol} is amplified by the ratio of the cross sections k_{A}.

For the realized prototype, the effect of the undesired d_{tol} is investigated more accurately with the aid of the 3-D FEM model. Already for $d_{\mathrm{tol}} = 0.1$ mm, estimated in Appendix B, the internal torque M_{in} is reduced by 40%. Consequently, the RA will require about three times the predicted ohmic losses to generate the nominal torque (i.e., $3 \times 0.1\ \mathrm{W} = 0.3\ \mathrm{W}$), which is still within the available losses budget. It is, therefore, clear that a tradeoff between manufacturing complexity and required ohmic losses exists. For the case at hand, the chosen stator construction is relatively simple to realize, and the additional losses it introduces are not critical as they are negligible compared to the total losses of the LiRA. For future designs or a different system where losses minimization could be a serious concern, a different stator construction solution shall be preferred, e.g., with extended teeth to be inserted in the stator core.

D. EXPERIMENTAL TEST BENCH

The experimental test bench shown in Fig. 15 is adapted from the one already used for the commissioning of the LA [17]. The torque sensor used is the *Rokubi* from *BOTA Systems*, which provides six-axis force/torque measurements and was already used to commission the LA [17]. Its measurement principle is based on resistive strain gauges, and about its z-axis, it can measure up to 12 N·m with a signal noise level of 0.5 mN·m. The torque to be measured for the experimental verification of the RA is in the 10 mN·m range, which is relatively low. If the complete mover is rigidly coupled to the sensor, a shaft and rotary bearings would be needed. However, as verified by preliminary tests, these would introduce parasitic axial torques due to friction, specially in the presence of strong radial attraction forces that exist between mover and stator [17]. A reasonable alternative is to measure the torque applied to a single rotor. As seen from Fig. 12(a), this is equivalent to the total internal torque $M_{\mathrm{in,tot}}(\varphi_{\mathrm{rot}})$ (i.e., applied to the complete mover), as long as the single rotor is axially aligned with the teeth of a rotary stator. A single rotor can be directly mounted to the torque sensor, with a very good transmission of the generated torque to it. On the test bench, as visible in the close-up of Fig. 15, this is done by gluing the rotor to a rigid plastic fixture, which is then tightly screwed to the sensor. Coupled to the sensor, a rotary positioning stage is used to precisely position the rotor down to a 0.1° resolution. Finally, a linear positioning stage is also used in order to adjust the rotor's position along the axial direction. The test bench can thus be used to measure the generated axial torque exerted by the fixed stator on the single rotor for different angular positions φ_{rot}.

VI. EXPERIMENTAL VERIFICATION

The experimental measurements conducted on the hardware prototype of the RA assembled into the complete LiRA are reported in this section. The verification includes measurements of the profile of the internal torque along the circumferential direction from which the (average) machine constant k_{m} is obtained. For the presented measurements, the test bench in Fig. 15 is used. The axial position of the rotor is fixed such that it aligns with the middle of the stator teeth. This corresponds to the condition $z_{\mathrm{mov}} = 4.5$ mm. As can be seen from the illustration in Fig. 11, for this axial position of the mover, the total torque is almost totally provided by one rotary stator. This way, as mentioned, the internal torque generated and applied to the single rotor is approximately equivalent to the total $M_{\mathrm{in,tot}}(\varphi_{\mathrm{rot}})$ that would be generated and applied to the complete mover (i.e., with two rotors). In order to obtain the average internal torque $M_{\mathrm{in,avg}}$, the angular position of the rotor φ_{rot} is adjusted in steps of 5° from 0° to 180°. This is sufficient, as $M_{\mathrm{in}}(\varphi_{\mathrm{rot}})$ has a period of 180° due to the machine geometry, as seen, e.g., from Fig. 12(a). For each angular position φ_{rot}, the torque sensor is calibrated after the rotor is positioned in order to cancel any parasitic torque and measure exclusively the internal one. Then, as visible from the exemplary measurements in Fig. 16(a), a slowly rotating stator field is generated by impressing the currents $i_{\{\mathrm{a,b,c}\},\mathrm{R}}$ in the RA winding with a fixed amplitude $\hat{I}_{\mathrm{rf}}$ and a low frequency $f_{\mathrm{rf}} = 0.04$ Hz. This way, a sinusoidally varying torque $M_{\mathrm{rf}}(t)$ is applied to the fixed rotor and measured by the torque sensor. The amplitude $\hat{I}_{\mathrm{rf}}$ is chosen such that the peak-to-peak amplitude of $M_{\mathrm{rf}}(t)$ is at least five times larger than the declared noise-free resolution of the torque sensor, which is specified as $M_{\mathrm{sens,nfr}} = 3$ mN·m. With $\hat{I}_{\mathrm{rf}} = 0.2$ A, a peak-to-peak amplitude of $2\,\hat{M}_{\mathrm{rf},02} \approx 20\ \mathrm{mN{\cdot}m} > 5\,M_{\mathrm{sens,nfr}}$ is expected. The amplitude of the measured torque wave $\hat{M}_{\mathrm{rf},02}$ is reported

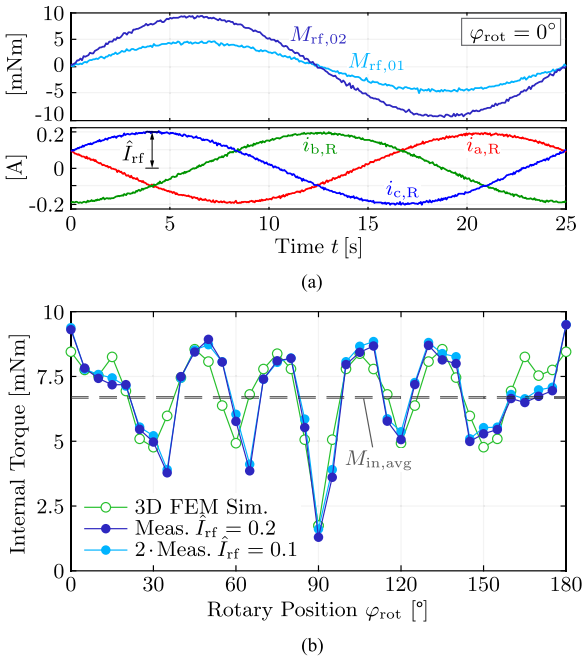

FIGURE 16. **(a) Exemplary measured torque profiles $M_{rf,\{02,01\}}(t)$ for the case $\varphi_{rot} = 0°$, generated by the slowly varying phase currents $i_{\{a,b,c\},R}$ with amplitude $\hat{I}_{rf} = \{0.2, 0.1\}$ A. (b) Internal axial torque profile for a single RA module, compared to the results of the 3-D FEM simulation with $N_R\hat{I}_R = 61$ Aturns. The results for $\hat{I}_{rf} = 0.1$ A are doubled for a direct comparison and verification of the torque linearity.**

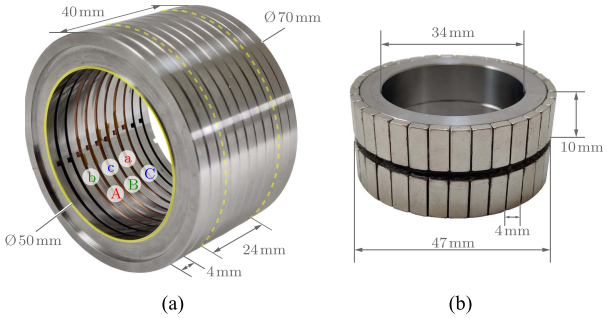

FIGURE 17. **Main parts of the realized hardware prototype of the LA of the *ShuttlePump* [17]. The stator consists of multiple ring segments made of *VACOFLUX50*, stacked together with six custom-made circular coils. The translator is realized with NdFeB PM segments (grade N50) glued on a *VACOFLUX50* back iron.**

in Fig. 16(b) for each angular position and compared to the results of the corresponding 3-D FEM simulations. As can be observed, the results are in good agreement with the simulation. The special shape of the torque profile due to the machine geometry with missing PMs is validated. Furthermore, in order to verify the linearity of the generated torque with respect to the impressed current, the measurements are also repeated with $\hat{I}_{rf} = 0.1$ A. The average absolute error of 11% is the result of mismatches in the torque profile at certain angular positions (e.g., $\varphi_{rot} = 35°$ or $65°$) that can be attributed to slight imperfections in the gluing of the PMs. Nevertheless, the average internal torque $M_{in,avg} = 6.75$ mN·m matches the simulated value, with an absolute error as low as 1.5%. From this result, the machine constant $k_m = M_{in,avg}/\hat{I}_{rf} = 33.75$ mN·m·A^{-1} is obtained. The (continuous) ohmic losses are then found as $P_{Cu} = 6\,R_c\,(M_{req}/k_m)^2 = 324$ mW.

VII. CONCLUSION

Next-generation TAHs need novel pumping principles and designs that could improve their durability and reliability. The *ShuttlePump* is an eloquent example, but, as seen, it comes at the cost of a more advanced and highly integrated LiRA drive system. In this article, the analysis, design, realization, and experimental verification of the RA of the *ShuttlePump* are presented. The experimental measurements verify that the proposed integrated RA concept is practically feasible and allows meeting the torque requirement of 3.1 mN·m with 324 mW of continuous power losses. Together with the estimated 8.7 W for the LA, this results in a total of 9 W for the whole LiRA.

With the two building blocks of the LiRA designed and experimentally verified, future work targets the operation of the complete drive system with full linear–rotary closed-loop position control. This requires the design and implementation of an embedded control system combining the previously designed eddy-current sensors [22] with a dedicated power electronics supply and control unit. The complete drive system then provides the basis for further testing of the *ShuttlePump* in vitro, i.e., on a dedicated hydraulic test bench, in order to finally assess whether the proposed concept can overcome the limitations of currently available TAHs and feature significant improvements concerning hemocompatibility (low blood trauma), durability, and safety.

APPENDIX A
OVERVIEW OF THE REALIZED LA

The analysis and design of the LA of the *ShuttlePump* were already presented in previous work by Giuffrida et al. [17]. Therefore, for the sake of completeness of this article, selected design choices and characteristics are reported in the following. The LA is designed as a tubular linear actuator (TLA) based on a PMSM. As can be observed from its section in Fig. 2, the stator is slotted with $N_s = 6$ slots, and the translator presents $N_p = 2$ poles, realized with radially magnetized surface-mounted permanent magnets. This pole–slot combination maximizes the winding factor of the PMSM. Furthermore, the presence of pole shoes on the stator teeth minimizes the cogging force along the axial direction. The stator of the basic TLA has an outer diameter $d_{out} = 70$ mm and its length is maximized to $l_{stat} = 40$ mm, according to the available space between inlets and outlets. The total length includes two side extensions as long as the stroke length $z_{strk} = 8$ mm. This measure is required in order to prevent strong edge cogging forces from appearing when the translator is displaced away from the center of the machine along the axial direction (i.e., out of the stator). The chosen PMSM

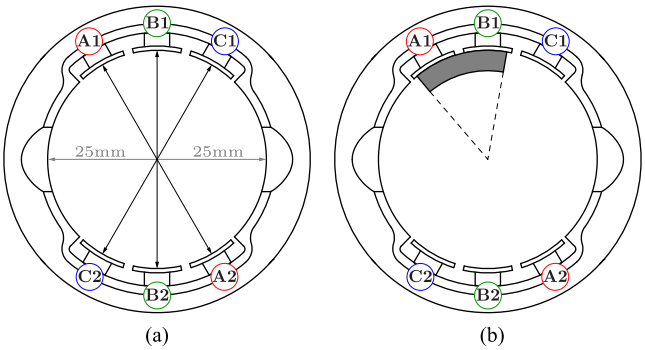

FIGURE 18. **(a) Measured inner radii of the RA to find the length of the introduced tolerance air gaps. (b) Indirect (magnetic) method to estimate the length of the introduced tolerance air gaps. Two teeth are magnetically shorted together with an arc-shaped piece of magnetic material, and the inductance of one of the coils in the magnetic circuit is measured.**

TABLE 5 **Measured Assembly Tolerance Air Gap Lengths (Direct Method)**

Tooth	r_{in} [mm]	d_{tol} [mm]	Tooth	r_{in} [mm]	d_{tol} [mm]
A1	24.809	0.191	A2	24.863	0.137
B1	24.739	0.261	B2	24.911	0.089
C1	24.839	0.161	C2	24.877	0.123

topology is optimized with the aid of FEM simulations. Special attention is dedicated to the strong radial reluctance pull forces acting on the translator as soon as it is not coaxial with the stator. This happens during operation due to the employed hydrodynamic bearing (instead of a mechanical one), which can only sustain a maximum radial load. The design offering the least average ohmic losses in the winding for the maximally allowed radial pull force is selected. The functionality of the realized hardware prototype, shown in Fig. 17, is verified experimentally. The results indicate that the operation of the LA respecting the axial motion profile with the specified axial force requirements needs $P_{\text{Cu,avg}} = 7.9$ W of ohmic losses and that the maximum radial pull is $F_{\text{rad}} = 23.8$ N for a $d_{\text{bg}} = 140$ µm off-centered translator.

APPENDIX B
MEASUREMENTS OF THE UNDESIRED AIR GAPS

In the following, the measurements of the undesired assembly tolerance air gap lengths, discussed in Section V-C, are reported. The air gap lengths are measured with two methods: a direct one (mechanical) and an indirect one (magnetic). For the first method, the inner radius of the tested RA module is measured at several locations, as indicated in Fig. 18(a). This is done using the measurement probe of the five-axis CNC machine *DMU 40 monoBlock* from *Deckel Maho*, which offers an accuracy of 5 µm. The difference with respect to the nominal $r_{\text{in}} = 25$ mm corresponds to the introduced tolerance air gap length d_{tol}. The measurements are reported in Table 5. For the second method, each tooth is made part of a magnetic circuit, where the tolerance gap is the main air gap. This is done by magnetically shorting two teeth against each other with a small piece of magnetic material, as shown in Fig. 18(b). This way, by measuring the inductance of a stator coil $L_{\text{meas,i}}$, the tolerance air gap length can be calculated as

$$d_{\text{tol,i}} = \frac{\mu_0 N_{\text{R}}^2 A_{\text{tooth}}}{2 L_{\text{meas,i}}}. \tag{7}$$

The measurements obtained with this method are reported in Table 6. Finally, an average value of $d_{\text{tol}} = 0.1$ mm is considered for Sections V-C and VI.

TABLE 6 **Estimated Assembly Tolerance Air Gap Lengths (Indirect Method)**

Connection	L [mH]	d_{tol} [mm]	Connection	L [mH]	d_{tol} [mm]
A1 to B1	10.02	0.107	A2 to B2	11.03	0.097
B1 to A1	9.89	0.109	B2 to A2	10.73	0.100
B1 to C1	10.08	0.107	B2 to C2	10.56	0.102
C1 to B1	12.34	0.087	C2 to B2	11.73	0.092

REFERENCES

[1] P. Ponikowski et al., "Heart failure: Preventing disease and death worldwide," *ESC Heart Failure*, vol. 1, no. 1, pp. 4–25, 2014.
[2] N. Conrad et al., "Temporal trends and patterns in heart failure incidence: A population-based study of 4 million individuals," *Lancet*, vol. 391, no. 10120, pp. 572–580, 2018.
[3] K. S. Shah, M. M. Kittleson, and J. A. Kobashigawa, "Updates on heart transplantation," *Curr. Heart Failure Rep.*, vol. 16, pp. 150–156, 2019.
[4] T. D. Ryan, J. L. Jefferies, F. Zafar, A. Lorts, and D. L. Morales, "The evolving role of the total artificial heart in the management of end-stage congenital heart disease and adolescents," *ASAIO J.*, vol. 61, no. 1, pp. 8–14, 2015.
[5] J. A. Cook et al., "The total artificial heart," *J. Thoracic Dis.*, vol. 7, no. 12, 2015, Art. no. 2172.
[6] G. Sunagawa, D. J. Horvath, J. H. Karimov, N. Moazami, and K. Fukamachi, "Future prospects for the total artificial heart," *Expert Rev. Med. Devices*, vol. 13, no. 2, pp. 191–201, 2016.
[7] B. P. Griffith et al., "Temporary use of the Jarvik-7 total artificial heart before transplantation," *New England J. Med.*, vol. 316, no. 3, pp. 130–134, 1987.
[8] K. Valeske, C. Yerebakan, M. Mueller, and H. Akintuerk, "Urgent implantation of the Berlin Heart Excor biventricular assist device as a total artificial heart in a patient with single ventricle circulation," *J. Thoracic Cardiovasc. Surg.*, vol. 147, no. 5, pp. 1712–1714, 2014.
[9] G. Torregrossa, A. Anyanwu, F. Zucchetta, and G. Gerosa, "SynCardia: The total artificial heart," *Ann. Cardiothoracic Surg.*, vol. 3, no. 6, pp. 612–620, 2014.
[10] R. D. Dowling et al., "The AbioCor implantable replacement heart," *Ann. Thoracic Surg.*, vol. 75, no. 6, pp. S93–S99, 2003.
[11] D. Timms, J. Fraser, M. Hayne, J. Dunning, K. McNeil, and M. Pearcy, "The BiVACOR rotary biventricular assist device: Concept and in-vitro investigation," *Artif. Organs*, vol. 32, no. 10, pp. 816–819, 2008.
[12] J. Glynn et al., "The OregonHeart total artificial heart: Design and performance on a mock circulatory loop," *Artif. Organs*, vol. 41, no. 10, pp. 904–910, 2017.
[13] F. A. Arabía et al., "Interagency registry for mechanically assisted circulatory support report on the total artificial heart," *J. Heart Lung Transplant.*, vol. 37, no. 11, pp. 1304–1312, 2018.
[14] F. D. Pagani, "Clinical implications of the total artificial heart: Adversity and progress," *J. Heart Lung Transplant.*, vol. 37, no. 11, pp. 1298–1300, 2018.
[15] M. Granegger, T. Bierewirtz, M. Nicolai, and U. Kertzscher, "Blood pump," EU Patent WO/2022/049 166, Mar. 2022.
[16] T. Bierewirtz et al., "A novel pumping principle for a total artificial heart," *IEEE Trans. Biomed. Eng.*, early access, doi: 10.1109/TBME.2023.3306888.
[17] R. V. Giuffrida et al., "Design and realization of a highly-compact tubular linear actuator for a novel total artificial heart," *IEEE J. Emerg. Sel. Topics Ind. Electron.*, vol. 4, no. 4, pp. 1010–1023, Oct. 2023.

[18] *Implants for Surgery—Active Implantable Medical Devices—Part 1: General Requirements for Safety, Marking and for Information to be Provided by the Manufacturer*, Standard ISO 14708-1:2000, Int. Org. Standardization, Geneva, Switzerland, 2000.

[19] T. Overboom, J. Jansen, E. Lomonova, and F. Tacken, "Design and optimization of a rotary actuator for a two-degree-of-freedom $z\phi$-module," *IEEE Trans. Ind. Appl.*, vol. 46, no. 6, pp. 2401–2409, Nov./Dec. 2010.

[20] J. Si, H. Feng, L. Ai, Y. Hu, and W. Cao, "Design and analysis of a 2-DOF split-stator induction motor," *IEEE Trans. Energy Convers.*, vol. 30, no. 3, pp. 1200–1208, Sep. 2015.

[21] K. Guo and Y. Guo, "Design optimization of linear-rotary motion permanent magnet generator with e-shaped stator," *IEEE Trans. Appl. Supercond.*, vol. 31, no. 8, 2021, Art. no. 0600705.

[22] R. V. Giuffrida, J. W. Kolar, and D. Bortis, "Eddy-current linear-rotary position sensor for an implantable total artificial heart," in *Proc. IEEE 25th Intern. Conf. Elect. Mach. Syst.*, Chiang Mai, Thailand, 2022, pp. 1–6.

[23] J. Cros and P. Viarouge, "Synthesis of high performance PM motors with concentrated windings," *IEEE Trans. Energy Convers.*, vol. 17, no. 2, pp. 248–253, Jun. 2002.

[24] A. Tüysüz, C. Zwyssig, and J. W. Kolar, "A novel motor topology for high-speed micro-machining applications," *IEEE Trans. Ind. Electron.*, vol. 61, no. 6, pp. 2960–2968, Jun. 2014.

[25] T. Taufer and L. Billet, "Compact BLDC & stepper motor technology for ultra-slim actuators," in *Proc. 10th ETG/GMM-Symp. Innov. Small Drives Micro-Motor Syst.*, 2015, pp. 1–6.

[26] M. Flankl, L. de Oliveira Baumann, A. Tüysüz, and J. W. Kolar, "Energy harvesting with single-sided linear induction machines featuring secondary conductive coating," *IEEE Trans. Ind. Electron.*, vol. 66, no. 6, pp. 4880–4890, Jun. 2018.

[27] K. Wang, J. Li, S. Zhu, and C. Liu, "Novel hybrid-pole rotors for consequent-pole PM machines without unipolar leakage flux," *IEEE Trans. Ind. Electron.*, vol. 66, no. 9, pp. 6811–6823, Sep. 2019.

[28] J. Li, K. Wang, and H. Zhang, "Flux-focusing permanent magnet machines with modular consequent-pole rotor," *IEEE Trans. Ind. Electron.*, vol. 67, no. 5, pp. 3374–3385, May 2020.

[29] Z. Zhu, Z. Azar, and G. Ombach, "Influence of additional air gaps between stator segments on cogging torque of permanent-magnet machines having modular stators," *IEEE Trans. Magn.*, vol. 48, no. 6, pp. 2049–2055, Jun. 2012.

[30] N. Leboeuf, T. Boileau, B. Nahid-Mobarakeh, N. Takorabet, F. Meibody-Tabar, and G. Clerc, "Effects of imperfect manufacturing process on electromagnetic performance and online interturn fault detection in PMSMs," *IEEE Trans. Ind. Electron.*, vol. 62, no. 6, pp. 3388–3398, Jun. 2015.